frontiers | Frontiers in Energy Research

TYPE Original Research
PUBLISHED 08 February 2024
DOI 10.3389/fenrg.2024.1361460

OPEN ACCESS

EDITED BY
Karunesh Kant,
Virginia Tech, United States

REVIEWED BY
Bo Jin,
Hunan University, China
Yongqing Xu,
Huazhong University of Science and Technology, China

*CORRESPONDENCE
Lei Liu,
csu_liu@csu.edu.cn

†These authors have contributed equally to this work and share first authorship

RECEIVED 26 December 2023
ACCEPTED 22 January 2024
PUBLISHED 08 February 2024

CITATION
Liu L, Xu W and Liu H (2024), Redox and melting characteristics of Mn-based ores for high-temperature thermochemical energy storage. *Front. Energy Res.* 12:1361460.
doi: 10.3389/fenrg.2024.1361460

Redox and melting characteristics of Mn-based ores for high-temperature thermochemical energy storage

Lei Liu[1]*†, Wenting Xu[2]† and Hanzi Liu[1]

[1]School of Energy Science and Engineering, Central South University, Changsha, China, [2]Xiangtan Iron and Steel Co., Ltd. of Hunan Valin, Xiangtan, China

Redox and melting characteristics of Mn-based ores were investigated to test their potential use in thermochemical energy storage (TCES). Two Mn-based materials (FJ and LY) were natural ores with the Mn content higher than 35 wt%, and one Mn-based material was prepared by adding an MgO–kaolin inert support into LY ores to increase its melting temperature. Cyclic reduction and oxidation reactivity of these Mn-based materials was studied via thermogravimetric analysis (TGA), and the melting behaviors of these materials were investigated by using a melting test setup with an optical camera–image system. It was found that the oxygen capacity of the FJ Mn ore can approach ~1.50 wt%, while the LY Mn ore had only 0.42 wt%–0.69 wt% oxygen capacity The deformation temperature of the FJ Mn ore is higher than that of the LY Mn ore, and the melting temperatures of the LY Mn ore can be significantly improved with the addition of an MgO–kaolin inert support, while the reactivity is decreased due to the addition of the MgO–kaolin inert material. This study proves that manganese ores with high oxygen capacity and deformation temperature have potential as TCES materials. For some manganese ores with low deformation temperatures, it is necessary to improve their melting temperatures and ensure oxygen capacity for high-temperature TCES applications.

KEYWORDS

thermochemical energy storage, manganese ore, melting behaviors, deformation temperature, MgO–kaolin

1 Introduction

The present global energy consumption is mainly based on the use of fossil fuels, which has contributed to many environmental problems. Renewable energy sources are considered attractive alternatives to replace fossil fuels because of their promising social, environmental, and economic benefits (Bilgen et al., 2004; Jin et al., 2023; Jin et al., 2024; Ouyang et al., 2024). The British Petroleum (BP) Company predicted that the consumption percentage of renewable energy sources will increase from 4% of its total primary energy consumption in 2016 to 14% in 2040 (British Petroleum Company, 2019). Solar energy is one of the most promising renewable energy resources as it is abundant and has the potential to provide energy with zero emission. Solar applications mainly comprise direct solar-to-electricity conversion by photovoltaics (PV) and solar-to-mechanical-to-electricity conversion by concentrated solar power (CSP). Both PV and CSP are needed to apply energy storage systems that are used for overcoming the inherent problems related to solar power intermittency. However, electrochemical energy storage for PV is more

expensive than thermal energy storage, which hampers the development of PV with energy storage (Weinstein et al., 2015; Feldman et al., 2016). Thermal energy storage (TES) systems play a vital role in the development of CSP plants. The solar energy intermittency can be solved by TES, in which intermittent solar energy is transformed to stable electricity to meet the electricity demand (Romero and Steinfeld, 2012; Pardo et al., 2014). In the TES systems, heat will be stored as sensible, latent, or thermochemical energy during periods of sunshine and released during periods of weak solar irradiation (Kuravi et al., 2013; Gil et al., 2010; Abedin and Rosen, 2011). Compared to sensible and latent heat storage operating at lower temperatures (<400°C and <500°C, respectively), thermochemical energy storage (TCES) based on completely reversible and rapid reactions, the suitable operating temperatures of which are 400°C–1,200°C, has aroused great attention for its potentially high thermal efficiency and compatibility with CSP technology (Abedin and Rosen, 2011; Agrafiotis et al., 2014; Yan et al., 2015; Prieto et al., 2016). Furthermore, the energy densities of the TCES systems are 5–10 times higher than those of the sensible and latent heat storage systems (Pardo et al., 2014). The first step to develop a TCES system is to select appropriate reaction patterns and then to study their chemical characteristics. Several reaction patterns have been proposed for TCES, including the metal hydride system (MH_n/M), metal hydroxide system ($M(OH)_2$/MO), metal carbonate system (MCO_3/MO), and metal oxide system (M_xO_y/M) (Yan et al., 2015; Kerskes et al., 2011; Chacartegui et al., 2016; Felderhoff and Bogdanović, 2009; Xu et al., 2021; Xu et al., 2022). The metal oxide system is considered particularly suited for CSP plants, which has good reaction reversibility and availability of air as the reactant and heat transfer fluid (Neises, et al., 2012).

Among the most studied metal oxides considered promising materials for TCES, manganese oxide is one of the most appropriate candidates (Carrillo et al., 2014a; Carrillo et al., 2014b; Carrillo et al., 2015a; Agrafiotis et al., 2016) as this material more abundant, less expensive, and non-hazardous among the proposed metal oxides. The redox reaction of manganese oxide can be described as follows:

$$6Mn_2O_3 \leftrightarrow 4Mn_3O_4 + O_2 \quad \Delta H = \frac{202\ \text{kJ}}{\text{kg}\ Mn_2O_3}.$$

In this perspective, the Mn_2O_3/Mn_3O_4 pair has been studied extensively, mostly on the milligram-scale of thermogravimetric analysis (Agrafiotis et al., 2016; Agrafiotis et al., 2017; Carrillo et al., 2014b; André et al., 2017), with some studies on lab-scale tests (Karagiannakis et al., 2014; Ströhle et al., 2016). However, the high temperature caused sintering in the redox cycle of manganese oxides due to the high temperature (Carrillo et al., 2014a; Carrillo et al., 2015b; Agrafiotis et al., 2017). In addition, the sintering phenomenon was also found in other metal oxide candidates, such as cobalt oxide and copper oxide (Block and Schmücker, 2016). The sintering process was reported to lead to an exponential thermal deactivation (Carrillo et al., 2014b), and the durability of the chemical reactivity of these materials is a key factor for long-term cycling of TCES. At present, research studies on the sintering problem are mainly focused on the doping inert support or other metal oxide materials to improve the sintering resistance of the materials (Carrillo et al., 2014a; Carrillo et al., 2014b; Carrillo et al., 2015b; Block and Schmücker, 2016; Wokon et al., 2017). In the study by Carrillo et al. (2015b), it was demonstrated that the addition of Fe_2O_3 to manganese oxides could stabilize and enhance the oxidation rate over long-term operations, which improves the sintering resistance in manganese oxides.

The TCES material prepared by the synthetic method normally has a high cost, and Mn-based natural ores have the advantages of rich reserves and low price (461 $/t) (Matzen et al., 2017) compared with synthetic Mn_2O_3 (about 100 €/kg) (Block and Schmücker, 2016). Natural materials with rich reserves and low prices are promising for large-scale application in the TCES system in order to decrease capital and operating cost. However, few research studies are currently being conducted on natural materials used as heat storage materials in the TCES system. At the same time, the issue of melting of TCES materials under TCES operational conditions is also a very important concern for material development because solar radiation can pass through the radiation window and heat the material to a very high temperature (Miller et al., 2016; Tescari et al., 2014). When the TCES material melts due to high operating temperatures, the window would be polluted, and the TCES system would collapse; therefore, it is necessary to investigate the melting characteristics of the TCES material.

In the present work, by using Mn-based natural minerals as thermochemical energy storage materials to decrease the cost, the reactivity and melting characteristics of Mn-based natural minerals were investigated. The purposes of this study were as follows: (1) natural Mn ores with a high Mn content were selected for the study, and one Mn ore was modified by adding an inert support to improve its melting temperature; (2) cyclic reduction and oxidation reactivity of these Mn-based materials were studied via TGA to provide oxygen capacity and kinetics; (3) a melting test setup with an optical camera-image system was applied to investigate the melting states of the materials to evaluate the effect of temperature on the material's melting behaviors.

2 Article types

2.1 Material preparation and characterization

Two low-cost raw manganese ores (named LY and FJ Mn ores) were selected and investigated as thermochemical heat storage materials. The Mn content is 38.11 wt% for FJ and 48.57 wt% for LY, and there is also substantial Fe content in both materials, as shown in Table 1. In order to increase the melting temperature of the LY ore, 9.98 wt% MgO and 9.98 wt% kaolin (MgO–kaolin inert support) were added into the LY raw material, and the prepared material was named LY–kaolin Mn ore. Therefore, three TCES materials were used for the test.

The above three materials are very fine powders and hence are not suitable for the TCES process; therefore, solid particles were prepared by rolling granulation in a micro-rotary furnace with a heater. First, the powders of raw manganese ores or LY–kaolin Mn ores were uniformly mixed in the rotating furnace for 1 h. Second, a dextrin solution acting as the organic binder was added to the powder, and a number of spherical particles were gradually formed in the micro-rotary furnace. The particle size can be controlled by adjusting the heating temperature and rotating speed. Third, after drying in air at room temperature for 10 h, the obtained spherical

TABLE 1 Composition of LY, FJ, and LY–kaolin Mn ores determined with XRF.

Name of Mn ore	Composition (wt%)									
	Mn	Fe	Si	Al	Na	K	P	Mg	Ca	Ti
FJ	38.11	10.08	3.63	1.81	0.895	9.45	0.24	0.22	0.89	0.17
LY	48.57	8.29	4.77	0.832	1.14	0.62	0.32	0.27	0.16	0.17
LY–kaolin	46.64	6.97	4.76	2.03	0.93	0.38	0.30	2.19	0.15	0.27

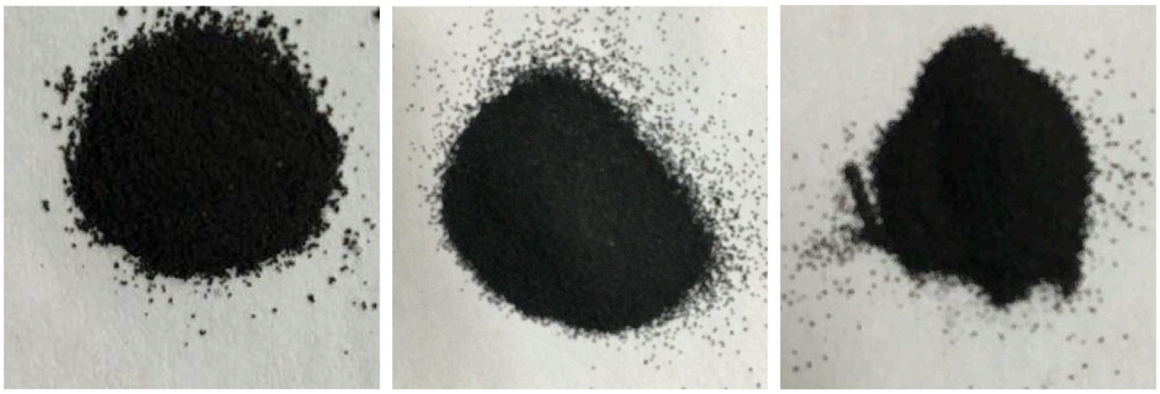

FIGURE 1
Photos of the prepared particles (left: FJ Mn ore, middle: LY Mn ore, and right: LY–kaolin Mn ore).

particles were calcined in air at 1,100 °C for 8 h, then cooled to 850°C, and calcined in air for 4 h to stabilize the structure. Finally, the spherical particles were crushed and sieved to the size range of 160–200 μm for the test. The prepared and sieved particles are shown in Figure 1. The samples were characterized by X-ray fluorescence (XRF) before being studied for redox cycles and melting behaviors. As shown in Table 1, all the samples are composed of Mn, Fe, alkali metal (K and Na), alkali earth metal (Ca and Mg), and other elements (mainly Si, Al, and P).

The three samples were characterized by X-ray diffraction (XRD) to identify the crystalline phases. XRD analysis was performed with Cu–Kα radiation (λ = 0.15406 nm) at room temperature, and the θ–θ symmetrical scans ranged from 10° to 90° with a step of 0.02°. The X-ray diffractograms were recorded and conducted through MDI Jade 6.0 software, and phase identification was aided by Powder Diffraction File (PDF). In addition, scanning electron microscopy (SEM, GeminiSEM 500) was applied to analyze the morphology of the samples before and after TGA redox cycles.

2.2 Redox experiment in TGA

Tests of reduction–oxidation cycles were carried out in a TG Q500 thermogravimetric analysis (TGA) instrument with a measurement accuracy of 0.001 mg. Signals of temperature and sample weight were continuously recorded by a data acquisition system connected to the TGA. Approximately 40 mg of the Mn ore sample was placed on an alumina crucible and subjected to 20 thermal cycles. Each cycle consisted of a heating step from 850°C to 900°C at 10°C min^{-1} for reduction under 100% N_2 flow of 100 mL min^{-1} and a cooling step from 900°C to 850°C at 10°C min^{-1} for re-oxidation under 20% O_2/80% N_2 flow of 100 mL min^{-1}.

2.3 Melting behavior experiment in a melting test setup with an optical camera–image system

A melting setup coupled with an optical camera–image system was used to determine the melting behaviors of the three Mn-based materials. A detailed description can be found in our previous work (Liu et al., 2019). As seen in Figure 2, the setup mainly consists of air sources, a computer, an optical camera–image system, a heating zone, and a thermocouple in the tube (I. D. 100 mm). The tube can be heated up to 1,550°C with 18°C min^{-1}. Before the melting characteristics test, the samples need to be prepared into cones by using a special designed mold, as shown in Figure 3. In each test, two sample cones were placed on the trays made in corundum, and then they were put into the heating zone together. During the experiment, an air stream (1 L min^{-1}) was introduced.

The cones would brighten when heated up to a certain temperature. A series of photos were continuously recorded by the optical camera–image system with 20 fps for following the shape of the cones. The following melting temperatures were introduced to describe the melting characteristics of the samples: (1) deformation temperature (DT), at which the top of the cones become round or bend due to melting phases in the tested samples; (2) softening temperature (ST), at which the cones are gradually bent until

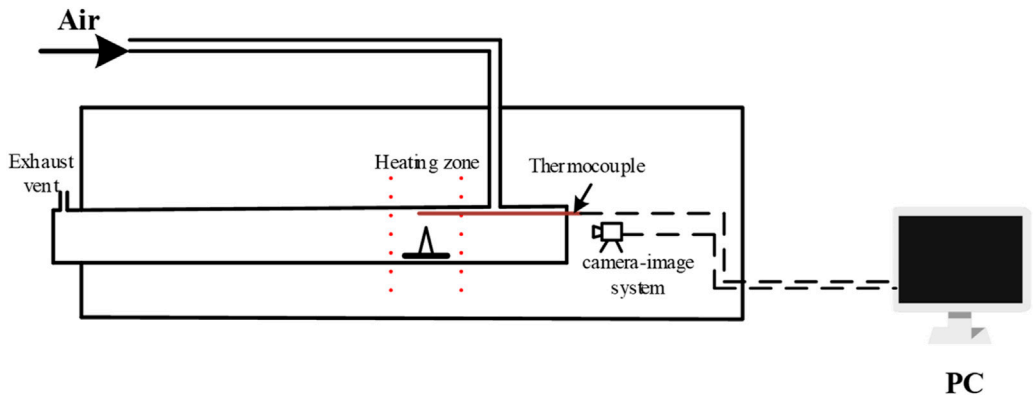

FIGURE 2
Melting test unit.

FIGURE 3
Schematic diagram of the tray and cone.

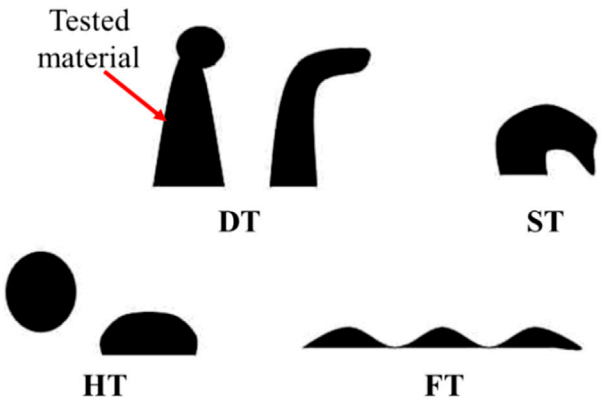

FIGURE 4
Judgment of melting characteristic temperatures.

touching the tray or the cones become spherical; (3) hemispherical temperature (HT), at which the cones melt and become approximately hemispherical; (4) flowing temperature (FT), at which the cones melt and expand to a layer less than 1.5 mm in height, as shown in Figure 4. These melting temperatures are indicators of the TCES operational temperature. The maximum temperature of TCES will be limited at less than the deformation temperatures (DT) of the materials for avoiding issues due to melting.

2.4 Data evaluation

Redox cycles of FJ, LY, and LY–kaolin Mn ores were conducted in TGA Q500, with altering gas atmospheres (20% O_2/80% N_2 and 100% N_2). Based on the weight change of the above three kinds of samples measured in each TGA redox cycle, the conversion of reduction and oxidation is defined as shown in Equations 1 and 2.

$$X_{re}(\%) = \frac{m_{ox} - m_t}{m_o} \times 100\%, \quad (1)$$

$$X_{ox}(\%) = \frac{m_t - m_{re}}{m_o} \times 100\%, \quad (2)$$

where X_{re} and X_{ox} are the reduction conversion and oxidation conversion, respectively, m_{ox} is the final mass after oxidation, m_{re} is the final mass after reduction, and m_t refers to the mass of the samples at time t. The theoretically maximum mass of released oxygen (m_o) is defined as in Equation 3.

$$m_o = m_s f_{Mn,s} M_O \frac{M_{Mn_2O_3}/2 - M_{Mn_3O_4}/3}{100 M_{Mn}}, \quad (3)$$

where m_s and $f_{Mn,s}$ refer to the total mass of the samples measured in TGA Q500 and the mass fraction of manganese in the tested samples determined by XRF. $M_{Mn_2O_3}$, $M_{Mn_3O_4}$, M_{Mn}, and M_O are the molar mass of Mn_2O_3, Mn_3O_4, Mn, and O, respectively. Here, it is assumed that manganese mainly exists in the form of Mn_2O_3 and Mn_3O_4 and the oxygen releasing process only occurs in the transformation of Mn_2O_3 to Mn_3O_4, considering that the decomposition of Mn_3O_4 happens at a higher temperature, such as 1,586°C (Zhang et al., 2016a; Zhang et al., 2016b).

3 Results

3.1 Oxygen capacity of natural Mn ores

A total of 20 reduction–oxidation cycles were monitored by TGA operating between 850°C and 900°C. The experimental results of FJ, LY, and LY–kaolin Mn ores are shown in Figure 5. The result was similar for each material. When the temperature was increased from 850°C to 900°C and maintained at 900°C under the N_2

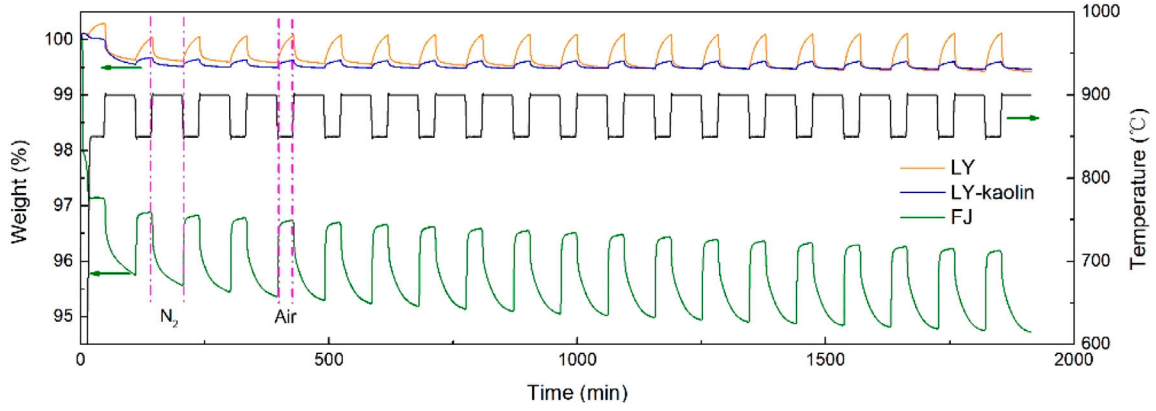

FIGURE 5
Thermogravimetric analysis (TGA) results of FJ, LY, and LY–kaolin Mn ores.

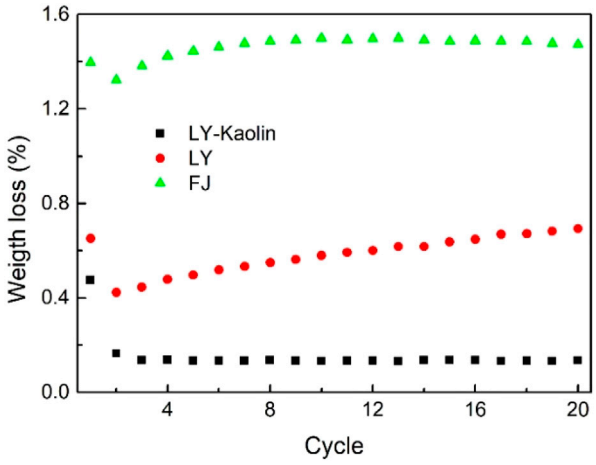

FIGURE 6
Stability of FJ, LY, and LY–kaolin Mn ores for 20 redox cycles.

condition, the weight of the samples decreased due to the release of oxygen (reduction); when the temperature was maintained at 850°C under the 20% O_2/80% N_2 condition, the weight of the samples increased due to re-oxidization. An obvious difference among the three materials is that the weight loss of the FJ Mn ore during the reduction is higher than that of LY and LY–kaolin Mn ores under the same experimental conditions. It can be seen from Figure 5 that when compared with the LY Mn ore and LY–kaolin Mn ore, the weight loss of the LY Mn ore during reduction is higher than that of the LY–kaolin Mn ore.

Figure 6 shows the stability of FJ, LY, and LY–kaolin Mn ores for 20 redox cycles. All three materials have experienced a decrease in the weight during their first cycle, as shown in Figure 6, and this is because some materials inside these natural ores decompose during the first cycle. For FJ, LY, and LY–kaolin Mn ores, the weight loss in the first cycle is 1.40%, 0.65%, and 0.47%, respectively; however, the weight loss is decreased to 1.32%, 0.42%, and 0.16% in the second cycle, respectively. As shown in Figure 6, the trends of reactivity change are different for FJ, LY, and LY–kaolin Mn ores from the second to twentieth cycles. The weight loss of the FJ Mn ore increases from 1.32% to 1.48% between the second and eighth cycle, and then the weight loss is maintained at around 1.50%. For the LY Mn ore, the weight loss increases from the second to twentieth cycles (0.42% to 0.69%). A different phenomenon for the LY–kaolin Mn ore is that its weight loss is maintained at 0.13 %–0.14% after the third cycle, and the oxygen capacity is very low. The FJ Mn ore has the highest oxygen capacity (1.50 wt%), followed by LY (0.69 wt%), while the oxygen capacity of the LY–kaolin Mn ore is the lowest (0.14 wt%). The oxygen capacity of the FJ Mn ore is 2.13 times that of the LY Mn ore and 10.5 times that of the LY–kaolin Mn ore in the twentieth cycle, as shown in Figure 6.

3.2 Reduction and oxidization kinetics of natural Mn ores

Figure 7 shows the reduction and oxidation kinetics of the FJ Mn ore at different cycles. It can be seen from Figure 7 that the reduction of the FJ Mn ore is divided into an initial fast reaction stage and a second slow reaction stage for each cycle. During the initial fast reaction stage, the conversion reaches 40% within 10 min, while it requires more than 50 min for the FJ Mn ore to reach 75% conversion, as shown in Figure 7A. There is almost no effect of cycle number on the reduction reactivity from the second to twentieth cycles. An initial rapid reaction stage and a second slow reaction stage are also observed in the oxidizing step of the FJ Mn ore for each cycle, as shown in Figure 7B. The oxidation kinetics is not affected by the number of cycles from the second to twentieth cycles. However, the oxidation conversion is low during the first cycle because some components could not be re-oxidized to their original state, as shown in Figure 5. The time for oxidization in the TGA test is not sufficient for the sample to fully oxidize due to the slow oxidization rate after the initial stage of each cycle.

Figure 8 shows the reduction and oxidation of LY Mn ore. A similar phenomenon is that the reducing process of the LY Mn ore is divided into a rapid reaction stage and a slow reaction stage for each cycle. The conversion improved from the fifth to twentieth cycles; for example, the reduction conversions of the fifth, tenth, fifteenth,

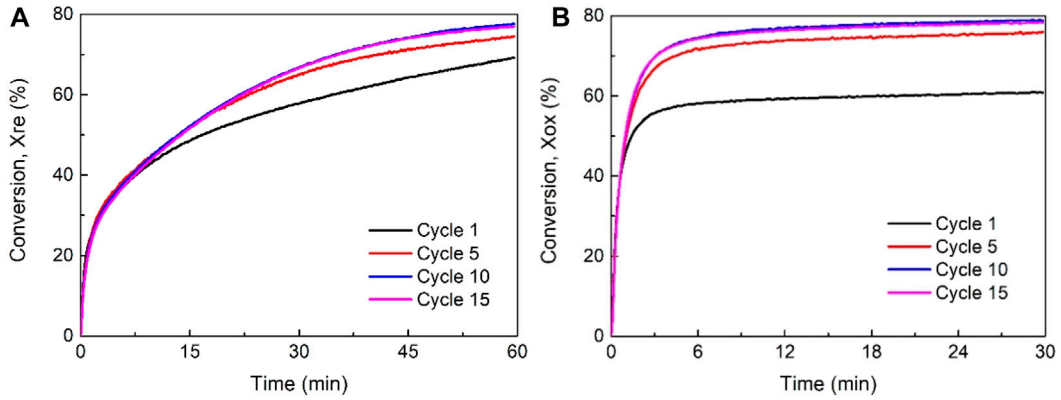

FIGURE 7
Reduction **(A)** and oxidation **(B)** conversion of the FJ Mn ore.

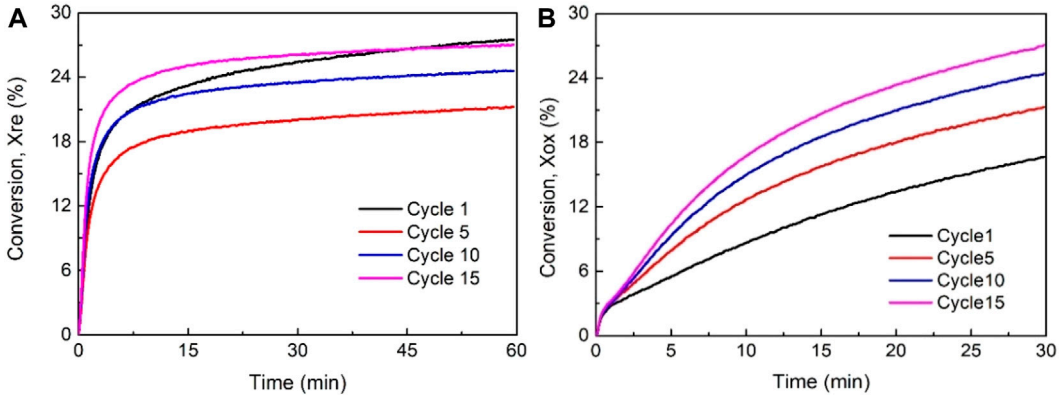

FIGURE 8
Reduction **(A)** and oxidation **(B)** conversion of the LY Mn ore.

and twentieth cycles are about 17.5%, 20%, 22.5%, and 25%, respectively. Although the manganese content of the FJ Mn ore is lower than that of the LY Mn ore, the conversion of reduction approaches 80%, and the oxygen capacity of the FJ Mn ore is 2.13 times than that of the LY Mn ore, as shown in Figure 6. The kinetic behavior of LY Mn ore oxidation is very different from that of the FJ Mn ore, and there are no so-called two stages as described in Figure 7B. The oxidation conversion of the LY Mn ore is increased from the fifth to twentieth cycles, but the samples could not be oxidized to their original state in the limited time; therefore, the oxidation conversion is low even though its Mn content is higher than that of the FJ Mn ore.

Figure 9 shows the comparison among these Mn ores. The fifteenth cycle was chosen compare the reduction and oxidization between the different samples. After mixing the LY Mn ore with kaolin and MgO, there is a big decrease in the oxygen capacity for the LY Mn ore, while the conversion of both reduction and oxidization could be improved, as observed in Figure 9. The LY–kaolin Mn ore shows the same features as the LY Mn ore in the initial stage (before 5 min) but becomes much quicker after 5 min. The final conversion levels of LY and LY–kaolin Mn ores are 27% and 35% in the fifteenth cycle, respectively, but the final conversion levels of LY and LY–kaolin Mn ores are still less than that of the FJ Mn ore, as shown in Figure 9. It also can be found that the oxidation conversion increased after mixing the LY Mn ore with kaolin and MgO. However, a similar phenomenon where the FJ Mn ore had a higher conversion than LY and LY–kaolin Mn ores could be observed in the oxidation stage, as shown in Figure 9. The kinetic behavior of LY–kaolin Mn ore oxidation also does not have the so-called two stages, which is same as for the LY Mn ore.

3.3 Particle characterization and morphology

The phase composition of prepared FJ, LY, and LY–kaolin Mn ores was analyzed by XRD, as shown in Figure 10. Both FJ and LY Mn ores consist of Mn_2O_3, Mn_3O_4, and other phases, and the LY-kaolin Mn ore also consists of Mn_2O_3, although the phase structures have some changes. The transformation between Mn_2O_3 and Mn_3O_4 is considered the effective reaction for heat storage. According to the XRD results, there exist some other Mn-

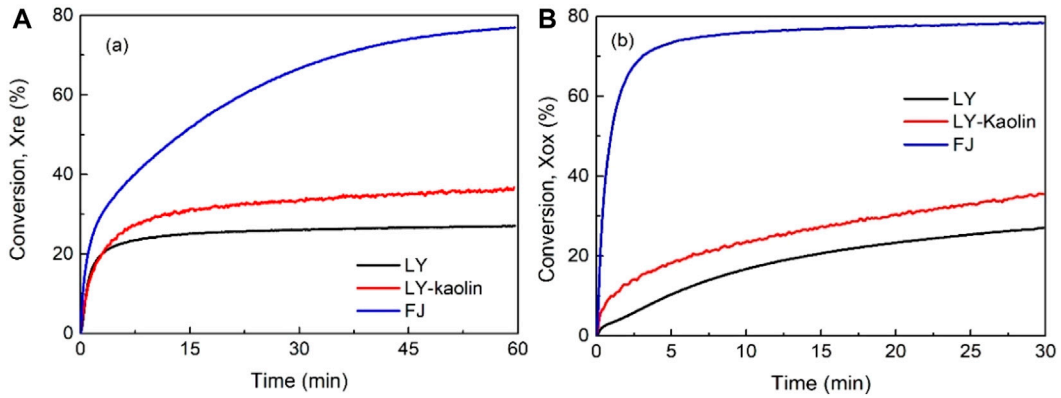

FIGURE 9
Reduction **(A)** and oxidation **(B)** conversion of FJ, LY, and LY–kaolin Mn ores at the 15th cycle.

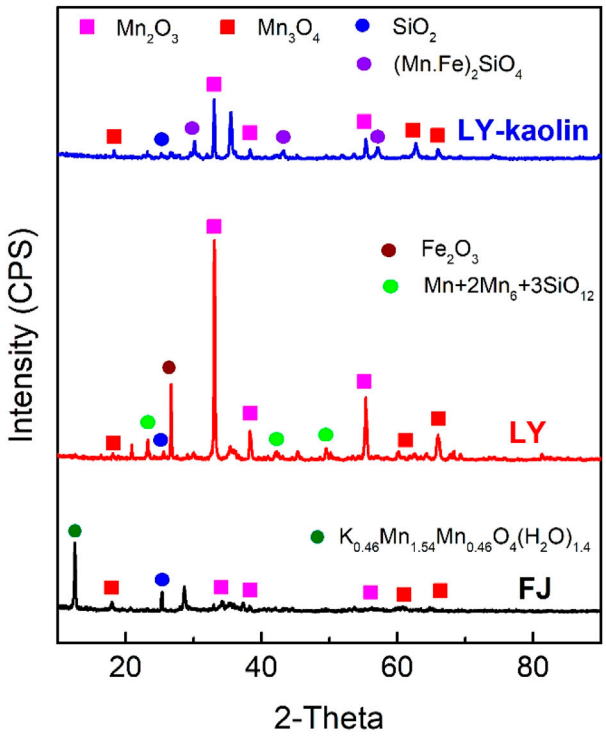

FIGURE 10
Main crystalline phases of the FJ Mn ore, LY Mn ore, and LY–kaolin Mn ore.

containing phases among FJ, LY, and LY–kaolin Mn ores, and these phases could not be reduced and oxidized in the experimental condition. Therefore, for all the samples, the conversion cannot reach 100%.

These materials before and after 20 redox cycles were examined by SEM analysis. SEM images of the particles present irregular shapes due to the crushing process during preparing of the particles. The values of weight loss of the FJ Mn ore are slightly decreased, which could be explained by the decreasing of pore space, as shown in Figure 11A. Conversely, as observed in Figure 11B, the surface of the LY Mn ore does not exhibit very dense morphology after TGA redox cycles. It means that the pore space increases after 20 reduction and oxidization reactions in TGA, which is in favor of gas diffusion inside the particles. Therefore, the LY Mn ore shows increasing oxygen releasing capacity, as demonstrated in Figure 6. As depicted in Figure 11C, the surface morphology of the used LY–kaolin ore did not show any significant change after 20 cycles, compared to the fresh samples. Therefore, increased physical stability of the particles will be obtained after the addition of the MgO–kaolin inert support.

3.4 Melting behaviors of natural Mn ores

The melting characteristics of these samples were investigated using the melting test unit setup, aiming for being helpful for controlling the operational temperature of the TCES system when using natural manganese ores as heat storage materials to avoid issues caused by melting. The melting behaviors of FJ, LY, and LY–kaolin Mn ores are shown in Figure 12, and for each sample, it was found that when the Mn-based samples were heated up to the deformation temperature, the conical material began to deform, slowly. The shape of the cones changed gradually with the increasing of the temperature, and after the shape experienced deforming, softening, and formation of hemispheres, the cones finally melted. For example, when the FJ Mn ore was heated to its deformation temperature (DT, 1,363°C), some phases/compositions had melted, leading to the top of the cone deforming and bending. With increasing temperature to softening temperature (ST, 1,418°C), more phases/compositions melted and the top of the cone touched the tray. Then, when heated up to hemispherical temperature (HT, 1,431°C), the tested materials showed a hemispherical shape. Finally, all the phases/compositions melted and the FJ Mn ore expanded to a thin layer at flowing temperature (FT, 1,462°C).

Figure 13 shows the melting temperatures of FJ, LY, and LY–kaolin Mn ores. The melting temperatures are very dependent on the Mn-based materials; for example, the deformation temperature (DT), softening temperature (ST), hemispherical temperature (HT), and flowing temperature (FT) of the LY Mn ore are 1,203°C, 1,256°C, 1,270°C, and 1,327°C,

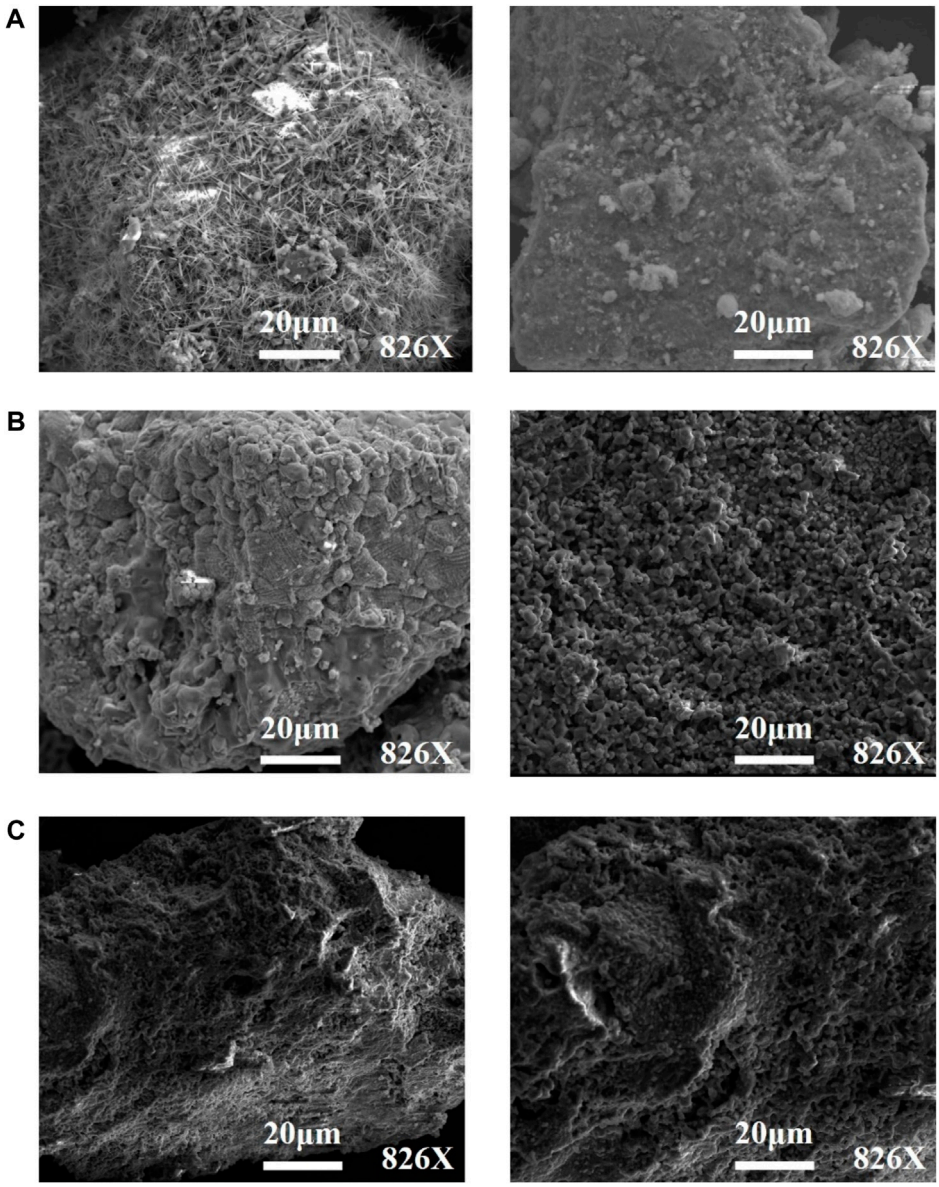

FIGURE 11
Morphology of the LY Mn ore **(A)**, FJ Mn ore **(B)**, and LY–kaolin **(C)** before (left) and after (right) TGA redox cycles.

respectively, while the corresponding melting temperatures of the FJ Mn ore are 1,363°C, 1,418°C, 1,431°C, and 1,462°C, respectively. It should be noted that these melting temperatures are indicators of the TCES system, the maximum temperature of the TCES system will be limited to 1,203°C for the LY Mn ore. The minimum and maximum threshold operational temperature for a CSP technology is 400°C and 1,200°C, respectively, and a higher temperature is desirable for the TCES system because of high thermal efficiency (André et al., 2016). The hot pot in the local zone could be existing when the TCES system operates at high temperature, caused by high radiation density and uneven radiation on the materials. This means that the TCES material will be heated at a very high temperature (Miller et al., 2016; Tescari et al., 2014). Therefore, the temperature of the hot pot could exceed the deformation temperature of the used material, such as the LY Mn ore. When the temperature of the hot pot is high enough (the temperature exceeds the deformation temperature), the low-melting-point eutectics at the surface of the materials would be melted. Then, the melting liquid would easily facilitate the formation of sintering when the particles touch together (Liu et al., 2019; Elled et al., 2013). Low-melting-point eutectics could also stain the radiation window of the TCES system, which damages the radiation window since the solar radiation cannot pass through the window and radiates on the heat storage materials, and a lot of solar radiation is absorbed by the radiation window. Therefore, as a serious consequence, the total collapse of the TCES system could occur, caused by sintering or damage of the window due to the increase in window temperature. For the FJ Mn ore, the TCES system can be operated at a relatively safer state because this FJ Mn ore has a high melting temperature, as shown in Figure 13.

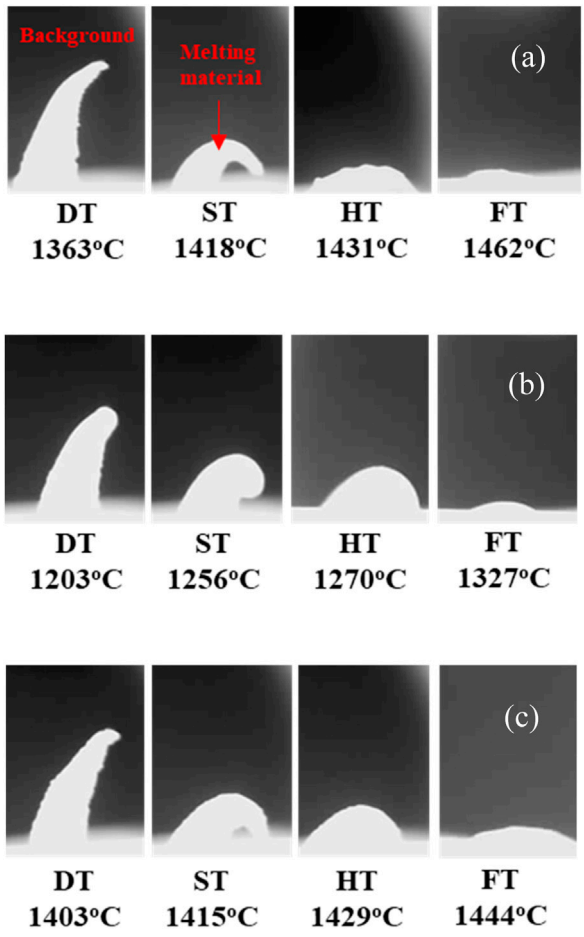

FIGURE 12
Melting behaviors of **(A)** FJ, **(B)** LY, and **(C)** LY–kaolin Mn ores.

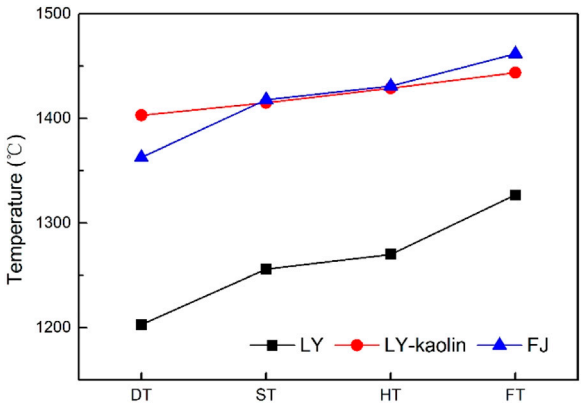

FIGURE 13
Melting temperatures of FJ, LY, and LY–kaolin Mn ores.

It was found that the melting temperatures increased substantially after adding the MgO–kaolin inert support to LY Mn ores, and the deformation temperature (DT), softening temperature (ST), hemispherical temperature (HT), and flowing temperature (FT) of the LY-kaolin Mn ore are 1,403°C, 1,415°C, 1,429°C, and 1,444°C, respectively. The deformation temperatures increased by 200°C due to the addition of the MgO–kaolin inert support. Therefore, the MgO–kaolin inert support is an effective additive for improving the melting temperature and resistance of the LY Mn ore, which could ensure that the TCES system works in a safe state for avoiding the issues caused by melting, when using the LY Mn ore as the heat storage material.

4 Discussion

Extensive efforts have been focused on the high purity of metal oxides and other synthetic materials to improve the physical or chemical performance of TCES materials. Table 2 provides the comparison of natural manganese ores with the main materials for TCES application, including the cost, oxygen capacity, and melting temperature. Material selection for TCES technologies is considered a complex process in large-scale application, and low-priced and non-toxic materials are preferable as candidate materials for TCES systems [12, 29, 37]. All the pure metal oxides have higher prices (60–250 €/kg) compared with natural manganese ores. Even if the MgO–kaolin pair and production process are considered, manganese ores are still very cheap (0.85 €/kg) for large-scale application. In addition, there is no environmental impact when selecting manganese ores as TCES materials. The melting issue should be considered a technical issue in TCES systems since the melting temperature of TCES materials is not high enough (Dizaji and Hosseini, 2018). Materials with low melting temperature are also prone to sintering. When comparing the melting temperatures between pure metal oxides and manganese ores, the melting temperatures of manganese ores are obviously higher. Therefore, manganese ores can decrease the risk of melting and sintering when heated to very high temperatures. Simultaneously, the MgO–kaolin pair is able to improve the melting temperature. Oxygen capacity is an indicator of reaction enthalpy and energy storage density. It can be concluded that the energy storage density of manganese ores is less than that of pure metal oxides. However, considering the advantages of low price and high melting temperature, natural manganese ores still have potential as TCES materials applied in large-scale TCES systems.

As mentioned in Sections 3.1 and Section 3.2, the FJ Mn ore has higher oxygen capacity and conversion of reduction and oxidation than LY and LY–kaolin Mn ores, and the melting temperature of the FJ Mn ore is also higher than that of LY and LY–kaolin Mn ores (as shown in Figure 13). Therefore, Mn-based natural ores with high oxygen capacity and high melting temperatures such as the FJ Mn ore are more suitable as a heat storage material than LY and LY–kaolin Mn ores when operating TCES systems at high temperature for higher efficiency. For Mn-based natural ores with lower melting temperatures, we should consider the effect of additives (such as the MgO–kaolin inert support) on material performance in improving melting temperatures in case of sintering or damage to the radiation window. However, oxygen capacity is decreased due to the use of additives. Therefore, further research about maintaining or even increasing the oxygen capacity of low-melting temperatures Mn-based nature ores while increasing melting temperatures should be conducted, such as impregnating

TABLE 2 Comparison of natural manganese ores with three types of pure metal oxides for TCES.

Material	Cost(€/kg)	Oxygen capacity (wt%)	Melting temperature (°C)	References
Co_3O_4/CoO	250	6.4	895	Agrafiotis et al. (2014); Block and Schmücker. (2016)
Mn_2O_3/Mn_3O_4	100	3.3	1,080	Carrillo et al. (2014a); Block and Schmücker. (2016)
CuO/Cu_2O	60	9.9	1,026	Block and Schmücker. (2016)
FJ Mn ore	0.55	1.5	1,363	This work
LY Mn ore	0.50	0.69	1,203	
LY–kaolin Mn ore	0.85	0.14	1,403	

Cu into Mn-based nature ores to improve the oxygen capacity (Xu et al., 2016; Xu et al., 2019).

5 Conclusion and outlook

Natural Mn-based ores (manganese ores) were studied using a thermogravimetric analyzer (TGA) and melting test setup with an optical camera–image system in order to investigate their potential use as thermochemical energy storage materials in the TCES system for CSP technology. The FJ Mn ore has the highest oxygen capacity (1.5%) compared to LY (max 0.69%) and LY–kaolin (0.14%). The FJ Mn ore also shows fast reduction and oxidization kinetics behavior and higher conversion than LY and LY–kaolin. The XRD result shows that only part of Mn content in the materials exists in Mn_2O_3/Mn_3O_4, which explains that the conversion cannot reach 100%. SEM analysis shows that the morphology of the FJ Mn ore becomes denser after redox cycles, and the pore space of the LY Mn ore increases. The FJ Mn ore presents higher melting temperatures than the LY Mn ore, and the deformation temperatures are 1,363°C and 1,203°C, respectively. It was demonstrated that adding the MgO–kaolin inert support to the LY Mn ore can improve the melting temperature substantially. This work proves that natural manganese ores have the potential to be used as TCES materials in large-scale application, in terms of cost reduction and resistance to sintering and melting. Further research on improving the oxygen capacity of low-melting temperature manganese ores modified by additives is required.

Data availability statement

The original contributions presented in the study are included in the article/Supplementary material; further inquiries can be directed to the corresponding author.

Author contributions

LL: conceptualization, funding acquisition, and writing–original draft. WX: formal analysis, investigation, methodology, and writing–original draft. HL: writing–review and editing.

Funding

The author(s) declare that financial support was received for the research, authorship, and/or publication of this article. This work is funded by the National Natural Science Foundation of China (52306178) and the Open Foundation of Key Laboratory of Energy Thermal Conversion and Control of the Ministry of Education.

Conflict of interest

Author WX was employed by Xiangtan Iron and Steel Co., Ltd. of Hunan Valin.

The remaining authors declare that the research was conducted in the absence of any commercial or financial relationships that could be construed as a potential conflict of interest.

Publisher's note

References

Abedin, A. H., and Rosen, M. A. (2011). A critical review of thermochemical energy storage systems. *Open Renew. Energy J.* 4 (1), 42–46. doi:10.2174/1876387101004010042

Agrafiotis, C., Block, T., Senholdt, M., Tescari, S., Roeb, M., and Sattler, C. (2017). Exploitation of thermochemical cycles based on solid oxide redox systems for thermochemical storage of solar heat. Part 6: testing of Mn-based combined oxides and porous structures. *Sol. Energy* 149, 227–244. doi:10.1016/j.solener.2017.03.083

Agrafiotis, C., Roeb, M., and Sattler, C. (2016). Exploitation of thermochemical cycles based on solid oxide redox systems for thermochemical storage of solar heat. Part 4: screening of oxides for use in cascaded thermochemical storage concepts. *Sol. Energy.* 139, 695–710. doi:10.1016/j.solener.2016.04.034

Agrafiotis, C., Roeb, M., Schmücker, M., and Sattler, C. (2014). Exploitation of thermochemical cycles based on solid oxide redox systems for thermochemical storage of solar heat. Part 1: testing of cobalt oxide-based powders. *Sol. Energy.* 102, 189–211. doi:10.1016/j.solener.2013.12.032

André, L., Abanades, S., and Cassayre, L. (2017). High-temperature thermochemical energy storage based on redox reactions using Co-Fe and Mn-Fe mixed metal oxides. *J. Solid State Chem.* 253, 6–14. doi:10.1016/j.jssc.2017.05.015

André, L., Abanades, S., and Flamant, G. (2016). Screening of thermochemical systems based on solid-gas reversible reactions for high temperature solar thermal energy storage. *Renew. Sust. Energy Rev.* 64, 703–715. doi:10.1016/j.rser.2016.06.043

Bilgen, S., Kaygusuz, K., and Sari, A. (2004). Renewable energy for a clean and sustainable future. *Energy sources.*, 26 (12), 1119–1129. doi:10.1080/00908310490441421

Block, T., and Schmücker, M. (2016). Metal oxides for thermochemical energy storage: a comparison of several metal oxide systems. *Sol. Energy* 126, 195–207. doi:10.1016/j.solener.2015.12.032

British Petroleum Company (2019). BP energy outlook 2019. https://www.bp.com/content/dam/bp/business-sites/en/global/corporate/pdfs/energy-economics/energy-outlook/bp-energy-outlook-2019.pdf.

Carrillo, A. J., Moya, J., Bayón, A., Jana, P., Romero, M., Gonzalez-Aguilar, J., et al. (2014a). Thermochemical energy storage at high temperature via redox cycles of Mn and Co oxides: pure oxides versus mixed ones. *Sol. Energy Mat. Sol. Cells.* 123, 47–57. doi:10.1016/j.solmat.2013.12.018

Carrillo, A. J., Serrano, D. P., Pizarro, P., and Coronado, J. M. (2014b). Thermochemical heat storage based on the Mn_2O_3/Mn_3O_4 redox couple: influence of the initial particle size on the morphological evolution and cyclability. *J. Mat. Chem. A* 2 (45), 19435–19443. doi:10.1039/C4TA03409K

Carrillo, A. J., Serrano, D. P., Pizarro, P., and Coronado, J. M. (2015a). Thermochemical heat storage at high temperatures using Mn_2O_3/Mn_3O_4 system: narrowing the redox hysteresis by metal co-doping. *Energy Procedia* 73, 263–271. doi:10.1016/j.egypro.2015.07.686

Carrillo, A. J., Serrano, D. P., Pizarro, P., and Coronado, J. M. (2015b). Improving the thermochemical energy storage performance of the Mn2O3/Mn3O4 redox couple by the incorporation of iron. *ChemSusChem* 8 (11), 1947–1954. doi:10.1002/cssc.201500148

Chacartegui, R., Alovisio, A., Ortiz, C., Valverde, J. M., Verda, V., and Becerra, J. A. (2016). Thermochemical energy storage of concentrated solar power by integration of the calcium looping process and a CO_2 power cycle. *Appl. Energy.* 173, 589–605. doi:10.1016/j.apenergy.2016.04.053

Dizaji, H. B., and Hosseini, H. (2018). A review of material screening in pure and mixed-metal oxide thermochemical energy storage (TCES) systems for concentrated solar power (CSP) applications. *Renew. Sust. Energy Rev.* 98, 9–26. doi:10.1016/j.rser.2018.09.004

Elled, A. L., Åmand, L. E., and Steenari, B. M. (2013). Composition of agglomerates in fluidized bed reactors for thermochemical conversion of biomass and waste fuels: experimental data in comparison with predictions by a thermodynamic equilibrium model. *Fuel* 111, 696–708. doi:10.1016/j.fuel.2013.03.018

Felderhoff, M., and Bogdanović, B. (2009). High temperature metal hydrides as heat storage materials for solar and related applications. *Int. J. Mol. Sci.* 10 (1), 325–344. doi:10.3390/ijms10010325

Feldman, D., Margolis, R., Denholm, P., and Stekli, J. (2016). *Exploring the potential competitiveness of utility-scale photovoltaics plus batteries with concentrating solar power*. NREL/TP-6A20-66592. Pittsburgh, PA: National Renewable Energy Laboratory.

Gil, A., Medrano, M., Martorell, I., Lázaro, A., Dolado, P., Zalba, B., et al. (2010). State of the art on high temperature thermal energy storage for power generation. Part 1—concepts, materials and modellization. *Renew. Sust. Energy Rev.* 14 (1), 31–55. doi:10.1016/j.rser.2009.07.035

Jin, B., Wang, R., Fu, D., Ouyang, T., Fan, Y., Zhang, H., et al. (2024). Chemical looping CO_2 capture and in-situ conversion as a promising platform for green and low-carbon industry transition: review and perspective. *Carb. Capt. Sci. Tech.* 10, 100169. doi:10.1016/j.ccst.2023.100169

Jin, B., Wei, K., Fu, D., Ouyang, T., Fan, Y., Zhao, H., et al. (2023). Chemical looping CO_2 capture and in-situ conversion: fundamentals, process configurations, bifunctional materials, and reaction mechanisms. *Appl. Energy Combust. Sci.* 16, 100218. doi:10.1016/j.jaecs.2023.100218

Karagiannakis, G., Pagkoura, C., Zygogianni, A., Lorentzou, S., and Konstandopoulos, A. G. (2014). Monolithic ceramic redox materials for thermochemical heat storage applications in CSP plants. *Energy Pr°Cedia* 49, 820–829. doi:10.1016/j.egypro.2014.03.089

Kerskes, H., Bertsch, F., Mette, B., Wörner, A., and Schaube, F. (2011). Thermochemische energiespeicher. *Chem. Ing. Tech.* 11 (83), 2014–2026. doi:10.1002/cite.201100091

Kuravi, S., Trahan, J., Goswami, D. Y., Rahman, M. M., and Stefanakos, E. K. (2013). Thermal energy storage technologies and systems for concentrating solar power plants. *Prog. Energy Combust. Sci.* 39 (4), 285–319. doi:10.1016/j.pecs.2013.02.001

Liu, L., Li, Z., Li, W., and Cai, N. (2019). The melting characteristics of Vietnamese ilmenite and manganese ores used in chemical looping combustion. *Int. J. Greenh. Gas. Con.* 90, 102792. doi:10.1016/j.ijggc.2019.102792

Matzen, M., Pinkerton, J., Wang, X., and Demirel, Y. (2017). Use of natural ores as oxygen carriers in chemical looping combustion: a review. *Int. J. Greenh. Gas. Con.* 65, 1–14. doi:10.1016/j.ijggc.2017.08.008

Miller, J. E., Ambrosini, A., Babiniec, S. M., Coker, E. N., Ho, C. K., Al-Ansary, H., et al. (2016). High performance reduction/oxidation metal oxides for thermochemical energy storage (PROMOTES). *Energy Sustain.* 50220. V001T04A024. doi:10.1115/ES2016-59660

Neises, M., Tescari, S., de Oliveira, L., Roeb, M., Sattler, C., and Wong, B. (2012). Solar-heated rotary kiln for thermochemical energy storage. *Sol. Energy.* 86 (10), 3040–3048. doi:10.1016/j.solener.2012.07.012

Ouyang, T., Jin, B., Mao, Y., Wei, D., and Liang, Z. (2024). Control of strong electronic oxide-support interaction in iron-based redox catalysts for highly efficient chemical looping CO_2 conversion. *Appl. Catal. B Environ.* 343, 123531. doi:10.1016/j.apcatb.2023.123531

Pardo, P., Deydier, A., Anxionnaz-Minvielle, Z., Rougé, S., Cabassud, M., and Cognet, P. (2014). A review on high temperature thermochemical heat energy storage. *Renew. Sust. Energy Rev.* 32, 591–610. doi:10.1016/j.rser.2013.12.014

Prieto, C., Cooper, P., Fernández, A. I., and Cabeza, L. F. (2016). Review of technology: thermochemical energy storage for concentrated solar power plants. *Renew. Sust. Energy Rev.* 60, 909–929. doi:10.1016/j.rser.2015.12.364

Romero, M., and Steinfeld, A. (2012). Concentrating solar thermal power and thermochemical fuels. *Energy Environ. Sci.* 5 (11), 9234–9245. doi:10.1039/C2EE21275G

Ströhle, S., Haselbacher, A., Jovanovic, Z. R., and Steinfeld, A. (2016). The effect of the gas–solid contacting pattern in a high-temperature thermochemical energy storage on the performance of a concentrated solar power plant. *Energy Environ. Sci.* 9 (4), 1375–1389. doi:10.1039/C5EE03204K

Tescari, S., Agrafiotis, C., Breuer, S., de Oliveira, L., Neises-von Puttkamer, M., Roeb, M., et al. (2014). Thermochemical solar energy storage via redox oxides: materials and reactor/heat exchanger concepts. *Energy Procedia* 49, 1034–1043. doi:10.1016/j.egypro.2014.03.111

Weinstein, L. A., Loomis, J., Bhatia, B., Bierman, D. M., Wang, E. N., and Chen, G. (2015). Concentrating solar power. *Chem. Rev.* 115 (23), 12797–12838. doi:10.1021/acs.chemrev.5b00397

Wokon, M., Kohzer, A., and Linder, M. (2017). Investigations on thermochemical energy storage based on technical grade manganese-iron oxide in a lab-scale packed bed reactor. *Sol. Energy* 153, 200–214. doi:10.1016/j.solener.2017.05.034

Xu, L., Chen, S., Sun, H., Li, Z., and Cai, N. (2019). Experimental study of Cu-modified manganese ore for O_2 production in the CLC+CLOU scheme. *Fuel* 244, 69–75. doi:10.1016/j.fuel.2019.01.120

Xu, L., Sun, H., Li, Z., and Cai, N. (2016). Experimental study of copper modified manganese ores as oxygen carriers in a dual fluidized bed reactor. *Appl. Energy.* 162, 940–947. doi:10.1016/j.apenergy.2015.10.167

Xu, Y., Lu, B., Luo, C., Wu, F., Li, X., and Zhang, L. (2022). Na_2CO_3 promoted CaO-based heat carrier for thermochemical energy storage in concentrated solar power plants. *Chem. Eng. J.* 435, 134852. doi:10.1016/j.cej.2022.134852

Xu, Y., Zhang, T., Lu, B., Luo, C., Wu, F., Li, X., et al. (2021). Glycine tailored effective CaO-based heat carriers for thermochemical energy storage in concentrated solar power plants. *Energy conver. manage.* 250, 114886. doi:10.1016/j.enconman.2021.114886

Yan, T., Wang, R. Z., Li, T. X., Wang, L. W., and Fred, I. T. (2015). A review of promising candidate reactions for chemical heat storage. *Renew. Sust. Energy Rev.* 43, 13–31. doi:10.1016/j.rser.2014.11.015

Zhang, H., Baeyens, J., Caceres, G., Degreve, J., and Lv, Y. (2016a). Thermal energy storage: recent developments and practical aspects. *Prog. Energy Combust. Sci.* 53, 1–40. doi:10.1016/j.pecs.2015.10.003

Zhang, H., Huys, K., Baeyens, J., Degrève, J., Kong, W., and Lv, Y. (2016b). Thermochemical energy storage for power generation on demand. *Energy Tech.* 4 (2), 341–352. doi:10.1002/ente.201500261